

Interplay of Orbital Degeneracy and Vacancies in Stabilizing Collinear Magnetic Order in $\text{Cr}_{1+\delta}\text{Te}_2$

Prasanta Chowdhury^{1,†}, Jyotirmoy Sau^{2,6,‡}, Mohamad Numan¹, Jhuma Sannigrahi³, Matthias Gutmann⁴, Gangadhar Das⁵, D. T. Adroja^{4,7}, Saurav Giri¹, Manoranjan Kumar², Subham Majumdar^{1*}

¹*School of Physical Sciences, Indian Association for the Cultivation of Science,*

2A & B Raja S. C. Mullick Road, Jadavpur, Kolkata 700 032, India

²*Department of Condensed Matter and Materials Physics,*

S. N. Bose National Centre for Basic Sciences, JD Block, Sector III, Salt Lake, Kolkata 700106, India

³*School of Physical Sciences, Indian Institute of Technology Goa, Farmagudi, Goa 403401, India*

⁴*ISIS Neutron and Muon Source, Science and Technology Facilities Council, Rutherford Appleton Laboratory, Chilton Didcot OX11 0QX, United Kingdom*

⁵*Elettra-Sincrotrone Trieste, Strada Statale 14 km,*

km 163.5 in AREA Science Park 34149, Trieste, Italy

⁶*Department of Physics and Astronomy, Uppsala University, Box-516, S-75120 Uppsala, Sweden and*

⁷*Highly Correlated Matter Research Group, Physics Department, University of Johannesburg, Auckland Park 2006, South Africa*

$\text{Cr}_{1+\delta}\text{Te}_2$, a two-dimensional van der Waals ferromagnet, displays a contested magnetic structure, poised between collinear and non-collinear spin configurations. In this work, we investigate the magnetic structure of $\text{Cr}_{1.33}\text{Te}_2$ at the microscopic level by combining single-crystal neutron diffraction, X-ray absorption spectroscopy, and first-principles calculations. Neutron diffraction measurements reveal a distinct collinear spin alignment, whereas spectroscopic analyses reveal inherent structural vacancies at both Cr and Te sites. These vacancies lead to local symmetry breaking that elevates the orbital degeneracy of the Cr 3d states, as demonstrated by our first-principles analysis. The resulting modification of magnetocrystalline anisotropy emerges as the key mechanism stabilising the collinear magnetic ground state over the non-collinear one in the presence of vacancies. Our findings uncover a vacancy-driven route to control spin anisotropy and magnetic ordering in layered ferromagnets, offering new insights into the design of tunable 2D magnetic materials.

Introduction: Vacancies play a decisive role in tuning the structural and magnetic properties of correlated materials, often inducing substantial changes in their magnetic ground states [1–3], yet their microscopic influence remains only sparsely investigated. Here we study one member of the $\text{Cr}_{1+\delta}\text{Te}_2$ ($0 \leq \delta \leq 1$) family of binary van der Waals (vdW) compounds, which is inherently prone to vacancy formation and thus provides a natural platform for revealing vacancy-driven modifications of magnetic structure. These materials provide a fertile ground for exotic spin textures, such as skyrmions and other non-coplanar spin configurations, which manifest in distinctive transport signatures, including the topological Hall effect (THE) [4–9]. The intercalated Cr concentration, δ , significantly influences the crystal structure, magnetic properties, and electronic transport characteristics of these compounds [6, 10, 11]. Studies have shown that as δ increases from 0.33 to 0.82, the magnetic Curie temperature (T_C) rises monotonically from 160 K to 350 K, accompanied by a transition in magnetic anisotropy from out-of-plane (OOP) to in-plane (IP) configurations [6, 12]. This magnetic anisotropy plays a crucial role in stabilizing the magnetic configurations in these compounds.

THE, which arises from non-coplanar spin configurations with finite scalar spin chirality (SSC), has been observed in several Cr-Te-based compounds [4, 6, 7, 13–15]. Recent studies using Lorentz Transmission Electron Microscopy (LTEM) have confirmed the presence of skyrmions in certain compositions, such as $\text{Cr}_{1.3}\text{Te}_2$ [5, 8], Cr_5Te_8 [7] and $\text{Cr}_{1.53}\text{Te}_2$ [6]. The existence of THE and skyrmions suggests non-collinear spin configurations in these systems. However, neutron diffraction studies have yet to fully elucidate the magnetic structures of $\text{Cr}_{1+\delta}\text{Te}_2$ compounds.

As shown in Fig. 1, we categorize the magnetic structures of Cr-Te-based binary compounds into two groups: collinear and non-collinear. Non-collinear structures are identified through theoretical predictions or experimental evidence, such as THE, skyrmion observations, neutron diffraction, or unconventional Anomalous Hall Effect (AHE) [4–8, 13–23]. In contrast, collinear structures are primarily determined by neutron diffraction and LTEM [8, 24, 25]. In particular, Fig. 1 reveals no clear correlation between the composition parameter δ and the magnetic structure. To date, neutron diffraction studies [8, 20–25] on $\text{Cr}_{1+\delta}\text{Te}_2$ have been limited, mostly conducted on powder samples, and the results for samples of identical composition often vary, as illustrated in Fig. 1. Thus, single-crystal neutron diffraction studies of $\text{Cr}_{1+\delta}\text{Te}_2$ are crucial for resolving these inconsistencies and clarifying its magnetic configurations.

Our neutron diffraction study on $\text{Cr}_{1.33}\text{Te}_2$, previously reported to show a Néel-type skyrmion and THE [5], unexpectedly revealed a collinear magnetic structure. EXAFS analysis revealed vacancies at Cr and Te sites, which,

* sspsm2@iacs.res.in; †These authors contributed equally to this work.

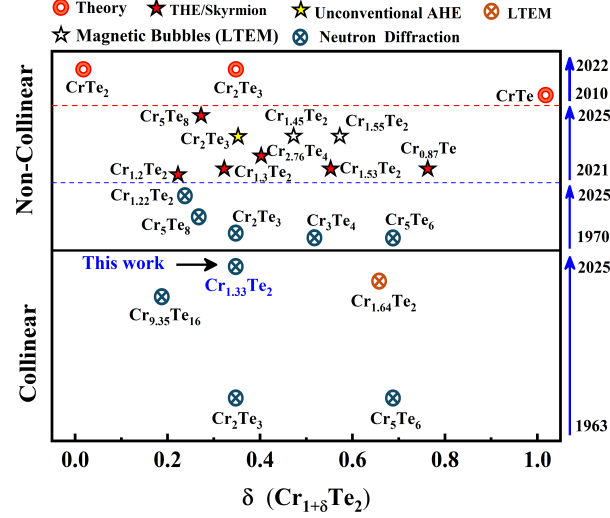


FIG. 1. Classification of magnetic structures in Cr-Te systems: collinear and non-collinear, based on theoretical and experimental study.

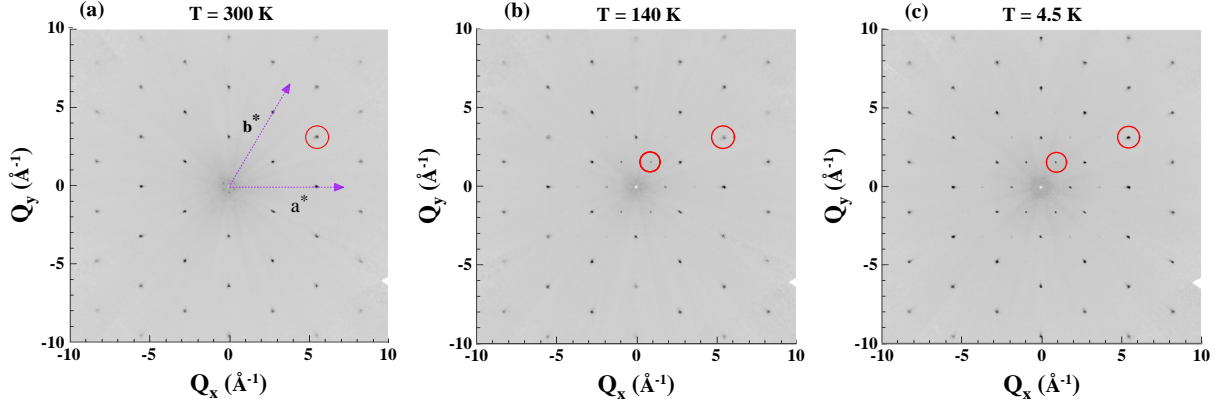


FIG. 2. (a), (b), and (c) show the $(h k 0)$ layer of $\text{Cr}_{1+\delta}\text{Te}_2$ measured on SXD at $T = 300, 140,$ and 4.5 K, respectively. Laue symmetry $3m$ has been applied.

combined with DFT calculations, indicated that orbital degeneracies significantly influence the magnetocrystalline anisotropy energy (MAE) [26–28]. In a vacancy-free system, orbital degeneracy favors a non-collinear spin arrangement, but vacancies disrupt the Cr-Te bonding, lifting d -orbital degeneracy and stabilizing a collinear magnetic state.

Single crystal neutron diffraction: High quality single crystals of $\text{Cr}_{1+\delta}\text{Te}_2$ ($\delta \approx 0.33$), used in this study, were synthesized by chemical vapor transport method (CVT) [29]. To accurately determine the magnetic ground state of $\text{Cr}_{1+\delta}\text{Te}_2$ and obtain a reliable magnetic propagation vector, temperature (T) dependent single-crystal neutron diffraction was performed on the SXD instrument [30] at the ISIS Facility, UK, using time-of-flight Laue technique to map the three-dimensional reciprocal space (see Appendix A). Fig. 2 (a)-(c) show the neutron diffraction patterns in the $(h k 0)$ scattering plane collected at $T = 300$ K, 140 K, and 4.5 K, respectively (180 and 90 K data given in Fig. 6 of Appendix C). The diffraction pattern at $T = 300$ K exhibits only the nuclear reflections permitted by the lattice symmetry of the $P\bar{3}m1$ space group (No. 164). Upon cooling below the transition temperature ($T_C = 191$ K), a distinct change in the intensity of several Bragg reflections is observed, arising from the onset of long-range magnetic order; selected reflections exhibiting intensity enhancement are marked by red circles Fig. 2. All magnetic reflections sit on the nuclear peak positions, indicating a commensurate magnetic structure with the propagation vector $\mathbf{k} = (0, 0, 0)$.

To elucidate the magnetic moment orientation, we examined the T dependence of the integrated intensities of the $(0 \bar{1} 0)$, $(0 0 \bar{1})$, and $(\bar{1} 1 0)$ Bragg peaks [Fig. 3]. The intensities of the $(0 \bar{1} 0)$ and $(\bar{1} 1 0)$ peaks increase upon cooling, following the M - T curve [Fig. 8 (a) of Appendix F], while the $(0 0 \bar{1})$ peak remains nearly T independent. Since

neutron scattering is sensitive only to the component of the magnetic moment perpendicular to the scattering vector, this behavior indicates that the magnetic moments are aligned along the c -axis. The result indicates the absence of appreciable spin canting upon cooling, contrasting with the canted magnetic structure reported for $\text{Cr}_{1.22}\text{Te}_2$ [20], but remains consistent with the collinear magnetic structure observed in $\text{Cr}_{12-x}\text{Te}_{16}$ [24].

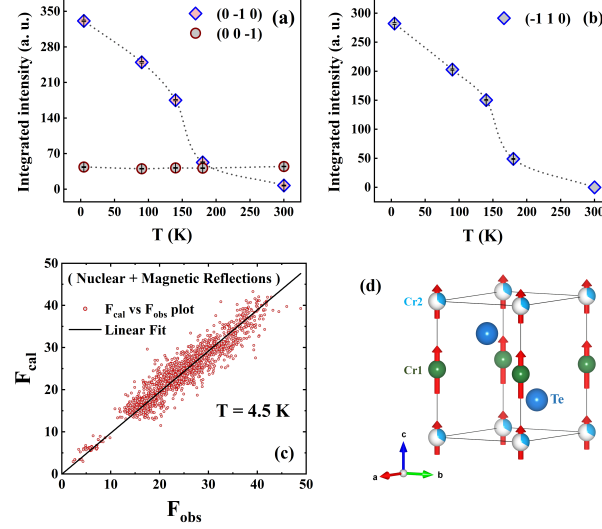


FIG. 3. (a), (b) Temperature evolution of integrated intensity of some selected Bragg peaks (0 -1 0), (0 0 -1) and (-1 1 0). (c) Calculated (F_{cal}) vs observed (F_{obs}) structure factors with linear fit at $T = 4.5$ K (nuclear+magnetic reflections) respectively. (d) Magnetic structure of $\text{Cr}_{1+\delta}\text{Te}_2$ at $T = 4.5$ K.

Based on the crystal symmetry and magnetic propagation vector \mathbf{k} , only four symmetry-allowed magnetic configurations are possible for $\text{Cr}_{1+\delta}\text{Te}_2$, as summarized in Table III of Appendix D. Among these, only the magnetic subgroup $P\bar{3}m'1$ (#164.89) permits a finite magnetic moment along the c -axis, consistent with the experimental observation. Consequently, the parent space group $P\bar{3}m1$ was used for nuclear refinement, and $P\bar{3}m'1$ for the combined nuclear and magnetic refinement. The results of the refinement for $T = 4.5$ K is presented as calculated (F_{cal}) versus observed (F_{obs}) structure factors with linear fits in Fig. 3 (c). Further refinement details are presented in Fig. 7 of Appendix E, and the corresponding refinement parameters and extracted magnetic moments are summarized in Table IV of Appendix E. We refine the moment of Cr1 and Cr2* separately at all the temperatures. At $T = 4.5$ K, an ordered moment values of $2.13(5) \mu_B/\text{Cr1}$ and $1.51(13) \mu_B/\text{Cr2}$ are obtained along the c -axis and the schematic of the magnetic structure at $T = 4.5$ K has been shown in Fig. 3 (d). The T dependence of the total ordered moment per unit cell, obtained from refinement, is shown in Fig. S3 (a) [31], alongside bulk magnetization data recorded under a 5 T applied field along the c -axis.

EXAFS: In contrast to X-ray and neutron diffractions, which provide information on the long-range crystallographic structure, EXAFS offers direct insight into the local atomic environment. To obtain quantitative information on the local atomic structure of $\text{Cr}_{1+\delta}\text{Te}_2$, the Cr K-edge EXAFS spectra were analyzed over the k -range of 3 to 13.2 \AA^{-1} (k denotes the wavenumber of the photoelectrons).

* In $\text{Cr}_{1+\delta}\text{Te}_2$, Cr has two inequivalent crystallographic sites, where Cr2 are the intercalated Cr with fractional occupancy residing between Cr1 and Te layers [29].

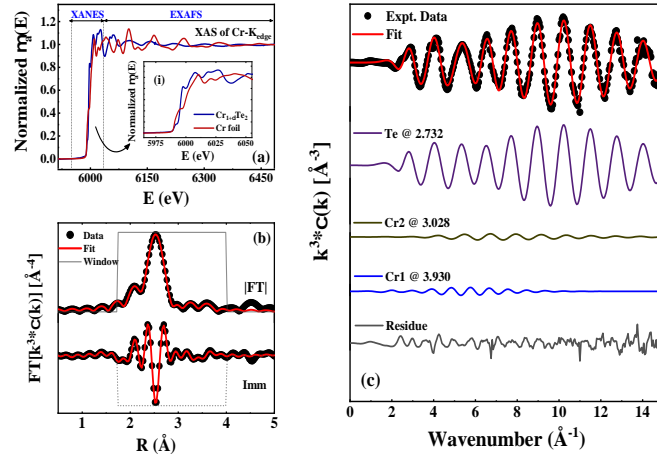


FIG. 4. (a) Normalized XAS spectra of $\text{Cr}_{1+\delta}\text{Te}_2$ and Cr foil measured at the Cr K-edge. The inset (i) shows the enlarge view of the XANES region. (b) Fourier transform of the experimental EXAFS data (black circles) along with the best-fit curve (solid red line). The magnitude ($|FT|$) and imaginary component (Imm) have been labeled and vertically shifted for clarity. (c) k^3 -weighted Cr K-edge EXAFS spectra in k -space (black circles) together with the corresponding best-fit curve (solid red line). The contributions from individual single-scattering paths, labeled by the scattering atom and its distance from the absorber.

TABLE I. The local structural parameters extracted from the EXAFS analysis at the Cr K-edge for $T = 300$ K are summarized. Here, N denotes the coordination number and σ^2 the Debye-Waller factor. The interatomic distances obtained from EXAFS fitting and from XRD refinement are listed as R and R_{XRD} , respectively. Parameters that were fixed or constrained during the fitting are indicated by the hash sign (#). The R -factor, which quantifies the degree of mismatch between the experimental data and the best-fit model, was found to be 0.0029.

Path	N [#]	$\sigma^2(\text{\AA}^2)$	$R(\text{\AA})$	$R_{\text{XRD}}(\text{\AA})$
Cr1-Te	4.5	0.0058 ± 0.0003	2.720 ± 0.003	2.732 ± 0.001
Cr1-Cr2	0.5	0.0064 ± 0.0055	2.937 ± 0.04	3.028 ± 0.000
Cr1-Cr1	4.5	0.0221 ± 0.0036	3.898 ± 0.021	3.930 ± 0.000

Fig. 4(a) shows the normalized XAS spectra [$\mu_a(E)$ vs. E^\dagger] of $\text{Cr}_{1.33}\text{Te}_2$, together with that of Cr foil, measured at the Cr K-edge and the inset shows an enlarged view of the XANES (X-ray Absorption Near Edge Structure) region. The rising line of the XANES spectra of $\text{Cr}_{1.33}\text{Te}_2$ is found to be shifted to higher energy compared to the data for the metallic Cr foil, indicating that Cr is in the higher oxidation state in $\text{Cr}_{1.33}\text{Te}_2$. Fig. 4(b) presents the Fourier transform of the EXAFS oscillations, displaying both the imaginary component and the modulus ($|FT|$), along with the corresponding best-fit curve in R -space. The EXAFS data were fitted using a multi-shell refinement procedure up to 4 \AA to extract structural information around Cr, covering the first three coordination shells. The scattering paths used to generate the theoretical spectra were calculated from the crystallographic structure of $\text{Cr}_{1+\delta}\text{Te}_2$ obtained from diffraction studies. The effective scattering amplitudes and phase shifts of the atoms were computed using the FEFF6 code [32] within the Artemis software package. Since two crystallographically distinct Cr sites are present, namely, Cr1 (fully occupied) and Cr2 (partially occupied), only the single-scattering paths involving nearest-neighbour Cr1-Te, next-nearest-neighbour Cr1-Cr2, and next-next-nearest-neighbour Cr1-Cr1 were considered in the analysis. The results of the EXAFS fitting are summarized in Table I. The k^3 -weighted best-fit spectra in k -space, together with the contributions from the individual single-scattering paths, are shown in Fig. 4(c). In the figure, the scattering paths are labeled according to the scattering atom and its distance from the absorber. For example, Te@2.732 indicates that the scattering atom is Te and it is at a distance of 2.732 \AA from the absorbing atom (here Cr1).

It is evident from Fig. 4(b) and (c) that the EXAFS signal is predominantly governed by the scattering contribution from the first nearest neighbour, namely the Cr1-Te single-scattering path. A key outcome of the present EXAFS analysis is the identification of vacancies at both Te and Cr sites, as summarized in Table I. In the ideal crystal structure

[†] E is the energy of the incident x-ray photon, and $\mu_a(E)$ is the x-ray absorption coefficient.

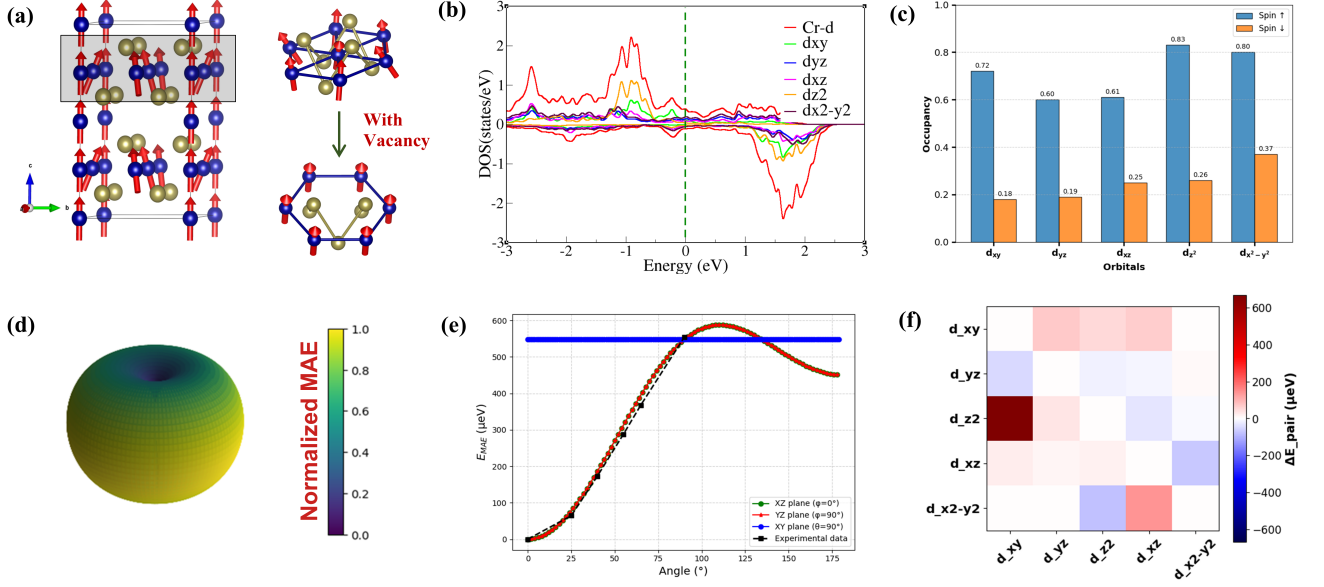


FIG. 5. (a) Magnetic configurations of $\text{Cr}_{10}\text{Te}_{16}$ ($\text{Cr}_{1.25}\text{Te}_2$) and vacancy-containing $\text{Cr}_8\text{Te}_{12}$ ($\text{Cr}_{1.33}\text{Te}_2$). The upper-right panel shows the zoomed layer of the vacancy-free system, while the lower panel depicts the favorable configuration with vacancy. (b) Partial density of states (PDOS) of Cr d orbitals for spin-up and spin-down channels. (c) Occupancy of different d orbitals for spin-up and spin-down channels. (d) Normalized magnetocrystalline anisotropy energy (MAE) in spherical polar coordinate space. (e) MAE in different planes as a function of the polar angle, along with the experimental data presented with black symbols and dotted line. (f) Orbital-pair resolved contributions to the MAE in the presence of SOC.

of $\text{Cr}_{1+\delta}\text{Te}_2$, each Cr1 atom is expected to be coordinated by six Te atoms in its first coordination shell; however, in the present case the coordination number is reduced to approximately 4.5 indicating significant Te vacancies. In the second coordination shell, the expected coordination number of about 0.66 for Cr2 atoms (arising from their fractional occupancy) is found to decrease to roughly 0.5. Similarly, vacancies are also evident in the third coordination shell.

Theoretical Study: EXAFS analysis reveals the presence of vacancies in the experimentally investigated $\text{Cr}_{1+\delta}\text{Te}_2$ ($\delta \approx 0.33$) sample. Motivated by this, we systematically examined the magnetic ground state under two representative conditions: (i) a pristine lattice without vacancies (WoV) and (ii) a defected lattice incorporating vacancies (WV). Further structural information can be found in Appendix H.

For the WoV configuration, first-principle calculations [33–35] indicate that a non-collinear spin arrangement, tilted from the $[0\ 0\ 1]$ direction at the $6i$ site, is energetically preferred, yielding a total energy of -150.7 eV [Fig. 5 (a), Fig. 10 of Appendix J]. While the corresponding collinear configuration (spins strictly aligned along the $[0\ 0\ 1]$ direction) lies marginally higher in energy by 0.1 eV, establishing the non-collinear state as the true magnetic ground state of the WoV phase.

In striking contrast, the energetic hierarchy reverses in the WV system. The non-collinear configuration at the $6i$ site no longer represents the ground state, exhibiting a total energy of -106.5 eV [Fig. 5(a) and Fig. 10 of Appendix J]. Instead, the collinear state becomes significantly stabilized, lying 2.2 eV lower (-108.7 eV) than the non-collinear counterpart. This pronounced energy gap signifies a strong preference for collinear magnetism in the presence of vacancies. To gain microscopic insight into the orbital physics of the Cr atom at the $6i$ site, we performed Wannierization [36, 37] to extract the onsite energies of the Cr d orbitals. The resulting onsite energies ϵ_i (Table VII of Appendix K) capture the effective orbital levels after incorporating the respective magnetic ground states. A close inspection of Table VII reveals a clear lifting of orbital degeneracy in the WV phase, which we attribute to symmetry reduction.

In the WoV trigonal phase ($P\bar{3}m1$), Te atoms reside in octahedral coordination with Cr (Fig. 11 of Appendix L). The threefold rotational symmetry along the c axis reduces the cubic O_h crystal field to D_{3d} , lifting the degeneracy of the t_{2g} (d_{xy} , d_{yz} , d_{xz}) manifold while leaving the e_g doublet (d_{z^2} , $d_{x^2-y^2}$) nearly unaffected. In contrast, for the WV case, induced by Cr-Te bond rupture, the local symmetry constraints are completely removed. Consequently, the five $3d$ orbitals evolve into fully non-degenerate states, exhibiting hybridized d_{z^2} , $d_{x^2-y^2}$, d_{xy} , d_{xz} , and d_{yz} characters. To unravel how these orbitals interact with spin and determine its orientation, we next analyze the magnetocrystalline anisotropy of the system. The MAE was evaluated within the second-order perturbation theory using the spin-orbit

coupling (SOC) Hamiltonian [38–40], as given in Eq. 1, where \mathbf{L} and \mathbf{S} denote the orbital and spin angular momenta of Cr.

$$H_{\text{SOC}} = \xi \mathbf{L} \cdot \mathbf{S} = \xi (L_x S_x + L_y S_y + L_z S_z), \quad (1)$$

where ξ denotes the SOC strength (0.0130 eV) [41, 42], $L_{x,y,z}$ are orbital angular momentum matrices in the d -orbital basis ($l = 2$), and $S_{x,y,z}$ are spin- $\frac{1}{2}$ operators.

Within this framework, the second-order SOC correction of the total energy for a spin quantization axis \hat{n} is expressed as

$$E^{(2)}(\hat{n}) = - \sum_{i \in \text{occ}} \sum_{j \in \text{unocc}} \frac{|\langle \psi_j | H_{\text{SOC}}(\hat{n}) | \psi_i \rangle|^2}{\varepsilon_j - \varepsilon_i}, \quad (2)$$

Detailed derivations are provided in Appendix M. The spin moment is governed by orbital occupancy, which scales with the numerator of Eq. 2. Orbital-resolved projected density of states (PDOS) calculations reveal that the redistribution of d -orbital occupations arises from the interplay between Hund’s exchange and the on-site Coulomb repulsion (Hubbard U) [see Appendix I]. The PDOS [Fig. 5 (b)] shows clear exchange splitting between spin-up and spin-down d orbitals, characteristic of a ferromagnetic ground state. Integration of the PDOS yields orbital occupancies [Fig. 5 (c)], displaying distinct filling asymmetries between the spin channels. Subsequently, SOC energies were computed for magnetization along the $[0\ 0\ 1]$ (z) and $[0.25\ -0.25\ 1.00]$ (\hat{n}) directions using Eq. 3.

The MAE is obtained as

$$\text{MAE} = E^{(2)}(\hat{n}) - E^{(2)}(z), \quad (3)$$

where a positive (negative) value corresponds to an easy axis along the z (\hat{n}) directions. The resulting magnetic anisotropy energy is $\text{MAE} \approx 550\ \mu\text{eV}$ [evaluated at $\theta = 90^\circ$; see Fig. 5(e)], indicating an easy axis along z ; however, in the WoV system, the sign reverses, signifying a reorientation of the easy axis toward \hat{n} [a detailed discussion is provided in Appendix M, N, O].

To construct the complete anisotropy landscape, we evaluated the SOC energies for magnetization orientations parameterized in spherical coordinates, $[\hat{S}(\Theta, \Phi) = (\sin \Theta \cos \Phi, \sin \Theta \sin \Phi, \cos \Theta)]$ with $\Theta \in [0, \pi]$ and $\Phi \in [0, 2\pi]$. The corresponding SOC energy is given by $[E^{(2)}(\Theta, \Phi) = E^{(2)}(\hat{S}(\Theta, \Phi))]$. For visualization, the energies were normalized between 0 and 1. Fig. 5 (d) presents the normalized 3D MAE surface, where the color gradient approaches blue near the z -axis, indicating a diminishing MAE magnitude.

To further elucidate the anisotropy behavior, we examined 2D cross-sections of the 3D MAE surface along the principal crystallographic planes (x - z , y - z , and x - y). As shown in Fig. 5(e), the MAE remains nearly constant at $\sim 550\ \mu\text{eV}$ across the x - y plane, while the energy minimum aligns with the z -axis. The measured MAE as a function of angle θ , extracted from the M - H curves at $T = 2.5\ \text{K}$, is in excellent agreement with the theoretical MAE curve for the x - z plane [Fig. 5(e)]. At $\theta = 90^\circ$, our measurements yield a MAE of $554\ \mu\text{eV}$, corresponding to an effective anisotropy constant of $K_{\text{eff}} = 14.6\ \text{J m}^{-3}$. This value of K_{eff} is consistent with those reported for bulk single crystals of $\text{Cr}_{1+\delta}\text{Te}_2$ [6] (see Appendix G). The microscopic origin of this anisotropy can be rationalized within the second-order perturbative framework, where SOC mediates virtual excitations between crystal-field-split orbitals. The pairwise anisotropy [40] contribution is expressed as

$$E_{ij} = \frac{f_i(1 - f_j)}{\varepsilon_i - \varepsilon_j} |\langle i | H_{\text{SOC}} | j \rangle|^2, \quad (4)$$

where f_i and ε_i are the occupation and crystal-field energy of orbital i , and $\langle i | H_{\text{SOC}} | j \rangle$ represents the SOC matrix element between orbitals i and j . This formulation captures how SOC-driven inter-orbital hybridization governs the anisotropy landscape, as illustrated in Fig. 5 (f).

The orbital-pair decomposition (Table II) reveals that the dominant contribution arises from the $d_{xy} \leftrightarrow d_{z^2}$ coupling, characterized by a small energy separation $\Delta \varepsilon \approx -0.05\ \text{eV}$ and a strong SOC matrix element $|H_n| \approx 1.8\ \text{meV}$. This strong hybridization between the in-plane (d_{xy}) and out-of-plane (d_{z^2}) orbitals generates the most substantial negative anisotropy term, favoring magnetization along the z -axis. In contrast, couplings involving the d_{xz} , d_{yz} and $d_{x^2-y^2}$ orbitals yield weaker contributions due to larger crystal-field splittings and reduced SOC-induced mixing. The absence of diagonal terms confirms that anisotropy arises purely from inter-orbital interactions [white region along diagonal in Fig. 5 (f)]. Collectively, these results demonstrate that the pronounced $d_{xy} \leftrightarrow d_{z^2}$ hybridization underlies the strong out-of-plane anisotropy, stabilizing magnetization along the $[0\ 0\ 1]$ direction. This orbital-selective SOC mechanism

TABLE II. Orbital-pair contributions (axis = [0, 0, 1])

orb_i	orb_j	$\Delta\varepsilon$ (eV)	$f_i(1 - f_j)$	$ \mathbf{H}_n $ (meV)	\mathbf{E}_{pair} (μeV)
d_{xy}	d_{z^2}	0.050	0.205	1.806	31.956
d_{xy}	d_{xz}	-0.150	0.257	1.475	-65.164
d_{yz}	$d_{x^2-y^2}$	-0.550	0.164	1.475	-7.576
d_{z^2}	d_{xy}	-0.050	0.300	1.806	-710.751
d_{z^2}	$d_{x^2-y^2}$	-0.350	0.226	1.806	-7.758
d_{xz}	d_{xy}	0.150	0.237	1.475	39.637
$d_{x^2-y^2}$	d_{yz}	0.550	0.354	1.475	18.968
$d_{x^2-y^2}$	d_{z^2}	0.350	0.266	1.806	88.318

offers a microscopic origin for the easy-axis behavior and underscores the pivotal role of specific $3d$ orbital couplings in governing the magnetic anisotropy of $\text{Cr}_{1+\delta}\text{Te}_2$.

Summary and Conclusions: Our single-crystal neutron diffraction study reveals that $\text{Cr}_{1.33}\text{Te}_2$ stabilizes in a collinear ferromagnetic structure, despite earlier reports observing Néel-type skyrmions and THE for this composition. Despite a seemingly well-ordered average structure, Cr K-edge EXAFS reveals the presence of both Te and Cr vacancies in the local environment. $\text{Cr}_{1.33}\text{Te}_2$ exhibits strong perpendicular magnetic anisotropy with easy c -axis, and together with theoretical calculations we found that vacancies play a decisive role in tuning the magnetic anisotropy and stabilizing the ground state magnetic structure from non-collinear to collinear. In conclusion, these findings establish a broadly applicable paradigm for engineering magnetocrystalline anisotropy and can help resolve the long-standing ambiguity in the magnetic structure of Cr-Te-based vdW systems. By exploiting crystal symmetries-such as the octahedral coordination presented here-to generate quasi-degenerate orbital manifolds, one can precisely tailor the MAE through controlled lifting of orbital degeneracy. This approach offers a unified framework for designing anisotropic magnetic behavior via symmetry-guided orbital engineering.

Acknowledgments: P.C. gratefully acknowledges the DST-INSPIRE program (Grant No. DST/INSPIRE Fellowship/2019/IF190532) for research assistance. We are thankful for the India-RAL collaborative project (Project No. SR/NM/Z-07/2015) for the neutron scattering studies at the ISIS facility, RAL, UK (Grant No. RB2410336 [43]). We also acknowledge Elettra Sincrotrone Trieste for providing access to its synchrotron radiation facilities with XAFS beamline. JS and MK acknowledge National Supercomputing Mission (NSM) for providing computing resources of ‘PARAM RUDRA’ at S.N. Bose National Centre for Basic Sciences, which is implemented by C-DAC and supported by the Ministry of Electronics and Information Technology (MeitY) and the Department of Science and Technology (DST), Government of India.

Appendix A: Experimental techniques

The detailed method for the growth of $\text{Cr}_{1+\delta}\text{Te}_2$ ($\delta \approx 0.33$) single crystals was discussed in our previous paper [29]. To probe the magnetic structure, a single crystal neutron diffraction experiment was carried out at the Single Crystal Diffractometer (SXD) beamline installed at the ISIS spallation neutron source, where the time-of-flight Laue technique is used to access large three dimensional (3D) volume of reciprocal space in a single measurement [30]. For the experiment a single crystal of approximate dimension $10 \times 2 \times 0.16 \text{ mm}^3$ (mass $\approx 40 \text{ mg}$) was attached to an aluminum (Al) pin using thin strips of adhesive Al tape. The sample was mounted on a closed-cycle refrigerator inside the evacuated sample tank and data were collected at temperatures $T = 4.5, 90, 140, 180$ and 300 K for several fixed crystal orientations. Data reduction was performed using SXD2001 software [44]. Nuclear and magnetic refinements were performed using JANA2020 software [45]. Magnetic measurements were carried out using the MPMS3 (SQUID magnetometer) from Quantum Design. Room-temperature X-ray absorption spectroscopy (XAS) at the Cr K-edge was carried out at the XAFS beamline of Elettra Sincrotrone Trieste, Italy [46]. The incident X-ray energy was selected using a Si(111) double-crystal monochromator. The EXAFS region of the acquired XAS data was processed and analyzed using the open-source DEMETER software package, which includes ATHENA and ARTEMIS [47, 48].

Appendix B: Sample characterization

$\text{Cr}_{1.33}\text{Te}_2$ has been characterized through single crystal and powder x-ray diffraction, transmission electron microscopy (TEM), magnetization measurements (see [29]). The powder and single-crystal XRD analysis confirmed that $\text{Cr}_{1+\delta}\text{Te}_2$ crystallizes in a trigonal structure belonging to the space group $P\bar{3}m1$ (No. 164) with no structural transition at low temperatures. The unit cell of $\text{Cr}_{1+\delta}\text{Te}_2$ contains two Cr sites, *i.e.*, Cr1 and Cr2. The Cr2 site has fractional occupancy and is intercalated in the van der Waals gap between two Cr1Te₂ layers. Magnetic measurements with the applied field (H) oriented along the c -axis and within the ab -plane reveal strong magnetic anisotropy, with the c -axis serving as the easy axis of magnetization. The temperature (T) dependence of magnetization (M) reveals a paramagnetic (PM) to ferromagnetic (FM) transition at approximately 191 K for both orientations.

Appendix C: Laue neutron diffraction pattern

Fig. 6(a), and (b) show the neutron diffraction patterns in the $(h k 0)$ scattering plane at $T = 180 \text{ K}$, and 90 K , respectively. The peaks marked with red circles show clear change in intensity with temperature (T).

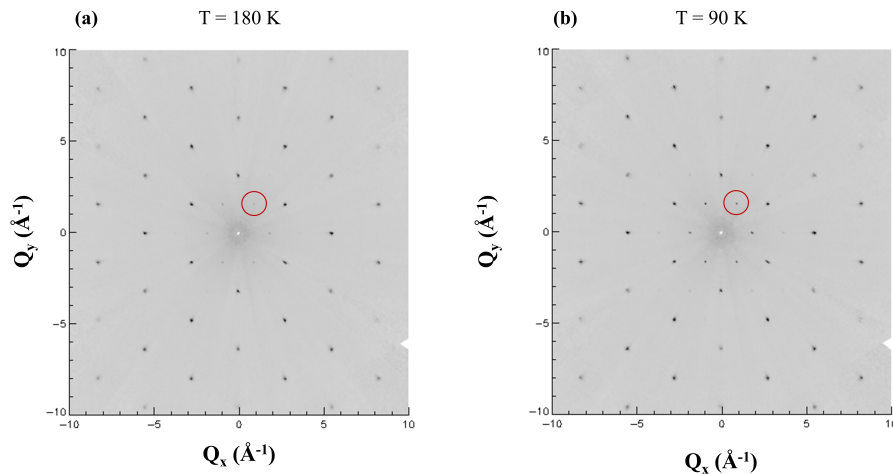


FIG. 6. (a), and (b) show the $(h k 0)$ layer of $\text{Cr}_{1+\delta}\text{Te}_2$ measured on SXD at $T = 180$, and 90 K , respectively. Laue symmetry $\bar{3}m$ has been applied.

Appendix D: Symmetry allowed magnetic structures

To determine the possible magnetic structures, a symmetry analysis was carried out using the MAXMAGN program available on the Bilbao Crystallographic Server [49, 50]. For this analysis, the crystallographic information file (CIF) of $\text{Cr}_{1+\delta}\text{Te}_2$ (as provided in Ref. [29]) was used, along with the experimentally observed magnetic propagation vector $\mathbf{k} = (0, 0, 0)$. The symmetry-allowed magnetic configurations corresponding to this setup are listed in Table III.

TABLE III. Symmetry-allowed magnetic moments for Cr sites in different magnetic space groups. Moment components are given as (M_x, M_y, M_z) .

Magnetic atoms	Allowed magnetic space groups			
	$P\bar{3}m'1$ (#164.89)	$P\bar{3}'m'1$ (#164.88)	$P\bar{3}'m1$ (#164.87)	$P\bar{3}m1$ (#164.85)
Cr1	(0, 0, M_z)	(0, 0, 0)	(0, 0, 0)	(0, 0, 0)
Cr2	(0, 0, M_z)	(0, 0, 0)	(0, 0, 0)	(0, 0, 0)

From Table III, it is evident that only the magnetic space group $P\bar{3}m'1$ permits a finite magnetic moment along the z axis, whereas the others yield zero moment. Hence, $P\bar{3}m'1$ was employed for the magnetic structure refinement.

Appendix E: Magnetic structure refinement

At $T = 300$ K, the nuclear structure refinement has been done using the $P\bar{3}m1$ space group and it is shown in Fig. 7 (a). Below T_C , the nuclear+magnetic structure refinement has been done using the space group $P\bar{3}m'1$ and the corresponding plots are shown in Fig. 7 (b)-(d) for $T = 180$ K, 140K, 90K. The ordered magnetic moments of the unit cell and individual Cr sublattices at different temperatures are listed in Table IV.

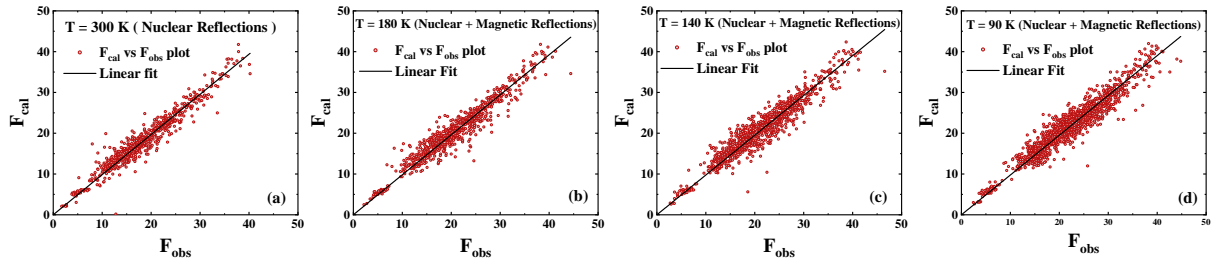


FIG. 7. (a)-(d) Calculated (F_{cal}) vs observed (F_{obs}) structure factors with linear fit at $T = 300$ K, 180 K, 140 K, 90 K, respectively.

Appendix F: Temperature dependent magnetic data

The T dependence of the total ordered moment per unit cell, obtained from refinement, is shown in Fig. 8 (a), alongside bulk magnetization data recorded under a 5 T applied field along the c -axis. Since a single unit cell contains one formula unit (f.u.) of $\text{Cr}_{1+\delta}\text{Te}_2$, the ordered moment per unit cell is equivalent to that per formula unit. As shown in Fig. 8 (a), the total ordered moment per unit cell exhibits a temperature dependence that closely resembles that of the bulk magnetization. The inset of Fig. 8 (a) shows the M vs. H data recorded at $T = 4.5, 90, 140, 180$ K. In Fig. 8 (b) the T variation of ordered moment of Cr1 and Cr2 has been shown. Interestingly, one can see that moment of Cr1 site increases monotonically with decrease in T , while the moment of intercalated Cr2 site initially decreases from 180 K and then started increasing below 90 K.

TABLE IV. Lattice parameters, refinement parameters and obtained magnetic moments (only M_z values)

Temperature (K)	Lattice parameters (in Å)	R-Factors	Individual Cr moments (M_z in μ_B)	Total moment in Unit Cell (M_z in μ_B)
4.5	a=b=3.946 c=5.998	$G.O.F=2.71$ R=7.62%, wR2=14.36%	Cr1=2.13(5) Cr2=1.51(13)	2.629(19)
90	a=b=3.944 c=6.006	$G.O.F=2.86$ R=7.36%, wR2=14.32%	Cr1=2.00(5) Cr2=1.05(14)	2.352(19)
140	a=b=3.941 c=6.028	$G.O.F=2.64$ R=7.54%, wR2=12.58%	Cr1=1.63(5) Cr2=1.17(15)	2.02(2)
180	a=b=3.938 c=6.039	$G.O.F=2.76$ R=7.11%, wR2=12.27%	Cr1=0.57(8) Cr2=1.7(2)	1.14(3)
300	a=b=3.935 c=6.070	$G.O.F=3.00$ R=7.00%, wR2=13.03%	-	-

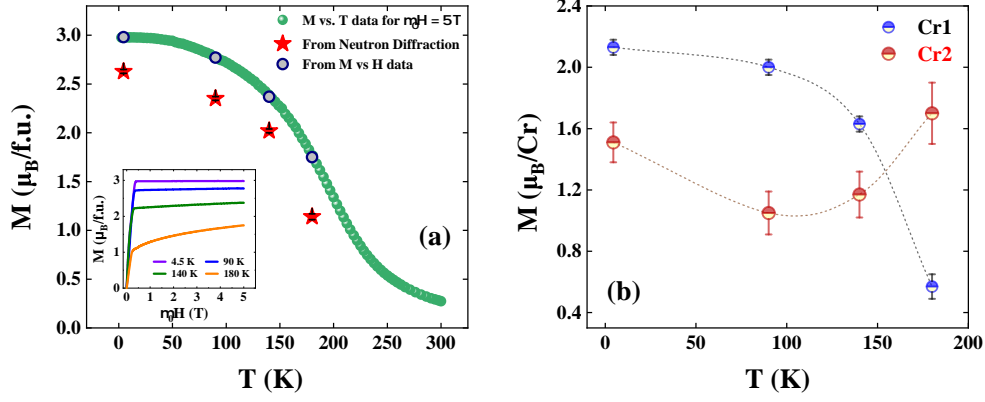


FIG. 8. (a) Main panel shows temperature variation of M as obtained from single crystal neutron diffraction (total moment) and bulk magnetization measurements. M vs T data taken at 5 T and the inset shows the M vs H curve at $T = 4.5, 90, 140, 180$ K (only 5 T values from it has been used in the main panel). (b) Temperature variation of ordered magnetic moment of Cr1 and Cr2 as obtained from neutron diffraction.

Appendix G: Perpendicular magnetic anisotropy

Fig. 9 (a) shows the field-dependent magnetization curves, measured at different angles ($\theta=0^\circ, 25^\circ, 40^\circ, 55^\circ, 65^\circ, 90^\circ$) with respect to the c -axis at $T=2.5$ K. From the figure it is evident that the sample exhibits strong perpendicular magnetic anisotropy (PMA) with c -axis being the easy axis of magnetization, which has also been discussed in our previous paper [29]. When measuring or calculating magnetic anisotropy, the demagnetization factor (shape anisotropy) correction to the applied field ($\mu_0 H^{\text{app}}$) should be considered to accurately determine the intrinsic anisotropy (e.g., magneto-crystalline anisotropy). After correction, the effective magnetic field ($\mu_0 H^{\text{eff}}$) inside the sample becomes:

$$\mu_0 H^{\text{eff}} = \mu_0 H^{\text{app}} - \mu_0 D M \quad (\text{G1})$$

where D is the demagnetization factor which is estimated to be $D_{ab}=0.097$ ($\mu_0 H^{\text{app}} \parallel ab, \theta=90^\circ$) and $D_c=0.8$ ($\mu_0 H^{\text{app}} \parallel c, \theta=0^\circ$). For $\theta=25^\circ, 40^\circ, 55^\circ, 65^\circ$ the D values are 0.6744, 0.5095, 0.3283, 0.2226 respectively. Now, if we have two M vs. H curves, one measured along the easy axis ($\theta=0^\circ$) and the other measured along different θ values, then the general anisotropy energy density difference between two directions can be expressed as:

$$\Delta E = K_{\text{eff}}[\sin^2 \theta - \sin^2 0^\circ] = K_{\text{eff}} \sin^2 \theta \quad (\text{G2})$$

Experimentally, this energy difference equals the area between the two M vs. H curves:

$$\Delta E = \mu_0 \int_0^{M_s} [H^{\text{eff}}(\theta; M) - H^{\text{eff}}(0^\circ; M)] dM \quad (\text{G3})$$

Thus the effective magnetic anisotropy K_{eff} can be calculated using the following relation [51, 52]:

$$K_{\text{eff}} = \frac{\mu_0 \int_0^{M_s} [H^{\text{eff}}(\theta; M) - H^{\text{eff}}(0^\circ; M)] dM}{\sin^2 \theta} \quad (\text{G4})$$

where M_s is the saturation magnetization (taken from the $\theta=0^\circ$ M vs. H curve). At $T = 2.5$ K, for $\theta=90^\circ$ K_{eff} calculated to be $14.6 \times 10^5 \text{ J m}^{-3}$, which shows excellent agreement with the earlier report on a nearly similar composition [6]. The change of K_{eff} with intercalated Cr concentration has been shown in Fig. 9(b) [obtained from [6, 12]]. The variation of K_{eff} with angle has been shown in the left panel of Fig. 9(c).

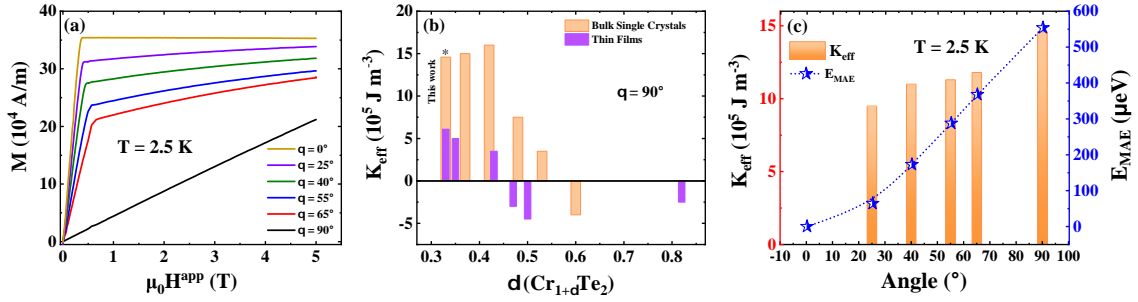


FIG. 9. (a) Field dependent magnetization curves measured at different θ values with respect to the c -axis at 2.5 K. (b) Variation of K_{eff} with intercalated concentration δ . The first column with star mark represent our calculated data and other data are taken from [6, 12]. (c) Left panel shows θ variation of K_{eff} and right panel shows θ variation magnetic anisotropy energy E_{MAE} .

The magnetic anisotropy energy is the energy required to rotate the magnetization from the easy axis to another direction (e.g., the hard axis). For a uniaxial system, with the easy axis perpendicular to the plane, the total anisotropy energy is often given by:

$$E_{\text{total}} = K_{\text{eff}} \cdot \sin^2 \theta \cdot V_{\text{uc}} \quad (\text{G5})$$

here V_{uc} is the unit cell volume. Taking $\theta=90^\circ$ (magnetization along the hard axis, in-plane) and $V_{\text{uc}}=80.88 \text{ \AA}^3$ (taken from diffraction study), the total anisotropy energy found to be approximately $E_{\text{total}}=7.37 \times 10^{-4} \text{ eV}$. As our unit cell has approximately 1.33 magnetic atoms ($n_{\text{mag}}=1.33 \text{ Cr}$), therefore the anisotropy energy per magnetic atom, $E_{\text{MAE}} = E_{\text{total}}/n_{\text{mag}} = 5.54 \times 10^{-4} \text{ eV} = 554 \mu\text{eV}$. The angle dependence of E_{MAE} has been shown in the right panel of Fig. 9(c) and it follows the theoretical curve very well [see Fig.5 (e) in the main text].

Appendix H: Theoretical study

As discussed in our previous paper [29], the supercell $\text{Cr}_{10}\text{Te}_{16}$ (equivalent to $\text{Cr}_{1.25}\text{Te}_2$) was used for the theoretical calculations [see Table V]; therefore, the theoretical magnetic investigations were also carried out on this composition. The possible magnetic structures corresponding to this composition as obtain from the MAXMAGN program are listed in the table VI. The magnetic space groups $P\bar{3}m1$ and $P\bar{3}m1$ are not permissible, as they constrain the moments to lie within the ab -plane. In case of $P\bar{3}'m'1$, the Cr3 and Cr4 sites carry no magnetic moment. Therefore, the investigation proceeds with $P\bar{3}m'1$, which has also been adopted for the experimental analysis. From table VI it is evident that Cr2 at the $6i$ site has a canted magnetic moment.

At first, systematic vacancies were introduced into the original cell ($\text{Cr}_{10}\text{Te}_{16}$) at both the Te and Cr sites, resulting in a final cell with the composition $\text{Cr}_8\text{Te}_{12}$ ($\approx \text{Cr}_{1.33}\text{Te}_2$). Subsequently, a systematic investigation of the magnetic ground state was carried out for two distinct cases: the system without vacancies (WoV) and the system with vacancies (WV).

TABLE V. Crystallographic information $\text{Cr}_{10}\text{Te}_{16}$ (equivalent to $\text{Cr}_{1.25}\text{Te}_2$): Space Group: $P\bar{3}m1$ (#164)

Atom	Label	Site	Sym.	x	y	z
Cr	Cr1	2c	3m.	0.00000	0.00000	0.25000
Cr	Cr2	6i	.m.	0.00000	0.50000	0.25000
Cr	Cr3	1a	$\bar{3}m.$	0.00000	0.00000	0.00000
Cr	Cr4	1b	$\bar{3}m.$	0.00000	0.00000	0.50000
Te	Te1	6i	.m.	0.33333	0.16667	0.12400
Te	Te2	6i	.m.	0.33333	0.16667	0.62400
Te	Te3	2d	3m.	0.33333	0.66667	0.12400
Te	Te4	2d	3m.	0.33333	0.66667	0.62400

Parameter	a (Å)	b (Å)	c (Å)	α (°)	β (°)	γ (°)
Value	7.85962	7.85962	12.11328	90.00	90.00	120.00

TABLE VI. Symmetry-allowed magnetic moments for Cr sites in different magnetic space groups. Moment components are given as (M_x, M_y, M_z) .

Magnetic atoms	Allowed magnetic space groups			
	$P\bar{3}m'1$ (#164.89)	$P\bar{3}'m'1$ (#164.88)	$P\bar{3}'m1$ (#164.87)	$P\bar{3}m1$ (#164.85)
Cr1	$(0, 0, M_z)$	$(0, 0, M_z)$	$(0, 0, 0)$	$(0, 0, 0)$
Cr2	$(M_x, -M_x, M_z)$	$(M_x, -M_x, M_z)$	$(M_x, M_x, 0)$	$(M_x, M_x, 0)$
Cr3	$(0, 0, M_z)$	$(0, 0, 0)$	$(0, 0, 0)$	$(0, 0, 0)$
Cr4	$(0, 0, M_z)$	$(0, 0, 0)$	$(0, 0, 0)$	$(0, 0, 0)$

Appendix I: Computational details

The electronic structure calculations were performed within density functional theory (DFT) using the Vienna *Ab-initio* Simulation Package (VASP) [33]. The interaction between ions and valence electrons was treated using the projector-augmented wave (PAW) method [34] with a plane-wave cutoff energy of 600 eV. Exchange–correlation effects were described within the generalized gradient approximation (GGA) [35], supplemented by an on-site Coulomb term (GGA + U) to account for electron correlation in the localized orbitals. The effective Coulomb interaction parameter U was varied between 0.5 and 0.8 eV to reproduce the experimental magnetic moments. Brillouin-zone integrations were performed using a Monkhorst–Pack $10 \times 10 \times 10$ k -point mesh. Structural relaxations were carried out until the forces on all atoms were below 0.001 eV/Å and the total energy converged within 10^{-6} eV.

Appendix J: Ground- and Excited-State Energy Landscapes of WoV and WV States

For the without-vacancy (WoV) and with-vacancy (WV) states, both collinear and non-collinear spin configurations were considered at the $6i$ site to examine the stability of magnetic states under spin-orbit coupling (SOC). In the collinear case, the spin quantization axis was fixed along the $[0\ 0\ 1]$ direction, while in the non-collinear case, the magnetic moment at the $6i$ site was oriented along $[0.25\ -0.25\ 1.00]$, as shown in Fig. 10.

The upper panel of Fig. 10 shows that, for the WoV case, the noncollinear configuration represents the true ground state of the system, whereas the lower panel indicates that, for the WV case, the collinear configuration is energetically favored.

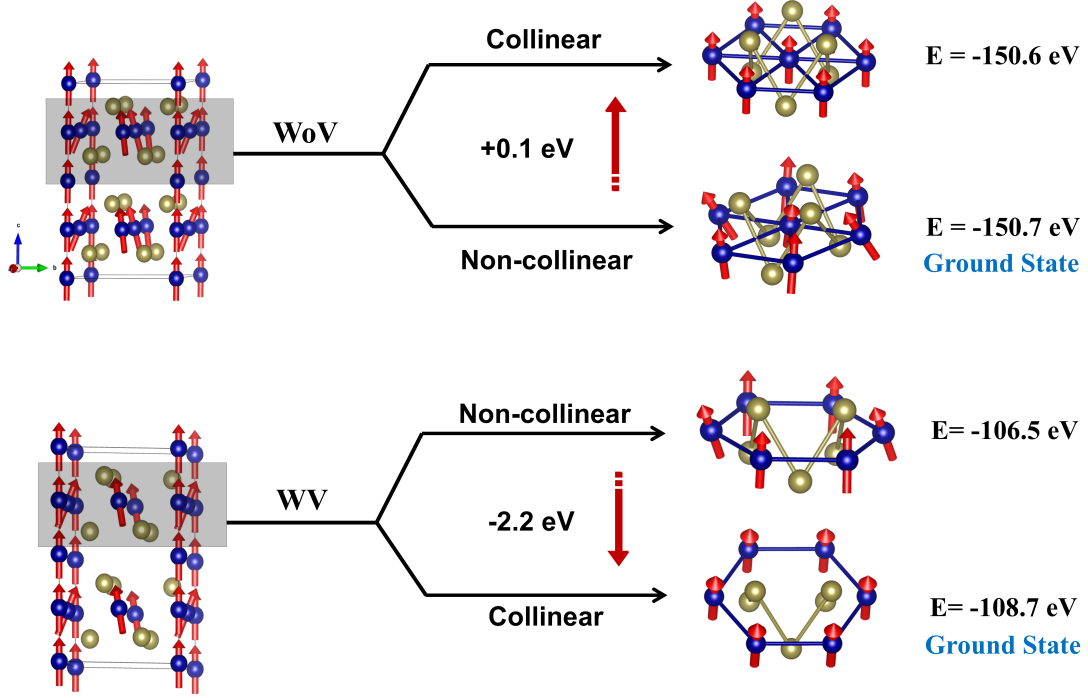


FIG. 10. The upper panel shows the favorable magnetic configuration for the system without vacancy *i.e.*, $\text{Cr}_{10}\text{Te}_{16}$. The lower panel shows the favorable magnetic configuration in presence of vacancy *i.e.*, for $\text{Cr}_8\text{Te}_{12}$.

Appendix K: Onsite energy extraction from Wannier functions

Onsite energy corresponding to a specific atomic orbital, we performed Wannierization of the Bloch wavefunctions using the maximally localized Wannier functions (MLWFs) framework [36, 37]. Starting from the Bloch eigenstates $\psi_{n\mathbf{k}}(\mathbf{r})$ calculated within density functional theory (DFT), we constructed Wannier functions via a unitary transformation in reciprocal space,

$$|w_{n\mathbf{R}}\rangle = \frac{V}{(2\pi)^3} \int_{\text{BZ}} d\mathbf{k} e^{-i\mathbf{k}\cdot\mathbf{R}} \sum_m U_{mn}^{(\mathbf{k})} |\psi_{m\mathbf{k}}\rangle, \quad (\text{K1})$$

where $U_{mn}^{(\mathbf{k})}$ is a gauge choice optimized to minimize the spread functional. The resulting Wannier Hamiltonian in real space is obtained as

$$H_{mn}(\mathbf{R}) = \langle w_{m0} | \hat{H} | w_{n\mathbf{R}} \rangle. \quad (\text{K2})$$

The onsite energy (ϵ_i) of a particular orbital localized on atom i is then identified as the diagonal matrix element of the Wannier Hamiltonian at the home cell ($\mathbf{R} = 0$),

$$\epsilon_i = H_{ii}(\mathbf{R} = 0). \quad (\text{K3})$$

The Bloch functions were constructed within the maximally localized Wannier function (MLWF) framework, using atomic-like Cr- d orbitals as initial projectors for 6i site's Cr in both cases.

Appendix L: Octahedral geometry

In Fig. 11 the octahedral geometry of Cr atom has been displayed before and after the introduction of vacancies. Here we specially focuses on the Cr atom at the 6i site, which has a canted magnetic moment.

	Orbital	ϵ_i (eV) WoV Case	ϵ_i (eV) WV Case
t_{2g} {	xy	4.6	5.2
	yz	5.3	4.95
	xz	4.6	5.15
e_g {	z^2	5.5	5.35
	$x^2 - y^2$	5.5	5.5

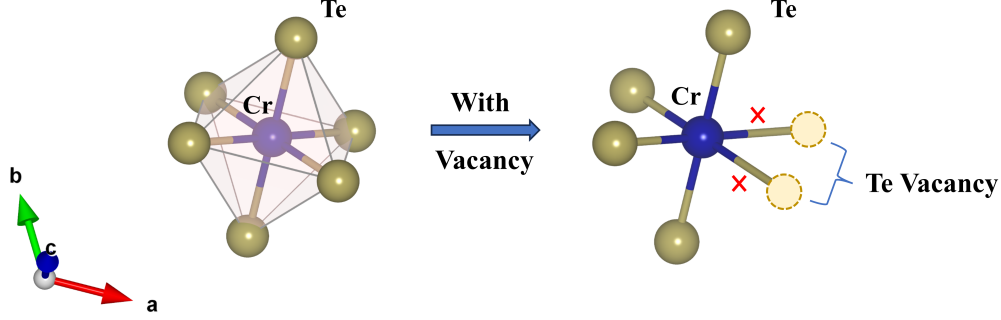
TABLE VII. Onsite energies (in eV) for WoV and WV cases for different d orbitals of Cr.

FIG. 11. Octahedral environment of Cr without and with vacancies

Appendix M: Perturbative Spin-Orbit Coupling Formalism for MAE

The magnetocrystalline anisotropy energy (MAE) was evaluated within second-order perturbation theory of the spin-orbit coupling (SOC) Hamiltonian [53, 54]. For an atom with orbital angular momentum \mathbf{L} and spin \mathbf{S} , the SOC Hamiltonian takes the form

$$H_{\text{SOC}} = \xi \mathbf{L} \cdot \mathbf{S} = \xi (L_x S_x + L_y S_y + L_z S_z), \quad (\text{M1})$$

where ξ is the SOC strength, $L_{x,y,z}$ are the orbital angular momentum matrices in the d -orbital basis ($l = 2$), and $S_{x,y,z}$ are the spin- $\frac{1}{2}$ operators.

The orbital angular momentum operators are constructed from the ladder operators,

$$L_+ |m\rangle = \sqrt{l(l+1) - m(m+1)} |m+1\rangle, \quad (\text{M2})$$

$$L_- |m\rangle = \sqrt{l(l+1) - m(m-1)} |m-1\rangle, \quad (\text{M3})$$

with

$$L_x = \frac{1}{2}(L_+ + L_-), \quad L_y = -\frac{i}{2}(L_+ - L_-), \quad L_z = \text{diag}(m), \quad (\text{M4})$$

for $m = -2, -1, 0, 1, 2$.

For a general magnetization axis \hat{n} , the SOC Hamiltonian is rotated via

$$H_{\text{SOC}}(\hat{n}) = R H_{\text{SOC}}(z) R^\dagger, \quad (\text{M5})$$

where $R = I_{\text{orb}} \otimes U$, with U the 2×2 spin rotation matrix

$$U = \exp[-i\theta(\hat{r} \cdot \mathbf{S})], \quad (\text{M6})$$

determined by the rotation aligning $z \rightarrow \hat{n}$.

The second-order SOC energy correction is then expressed as

$$E^{(2)}(\hat{n}) = - \sum_{i \in \text{occ}} \sum_{j \in \text{unocc}} \frac{|\langle \psi_j | H_{\text{SOC}}(\hat{n}) | \psi_i \rangle|^2}{\epsilon_j - \epsilon_i}, \quad (\text{M7})$$

where $|\psi_i\rangle$ and $|\psi_j\rangle$ are unperturbed d -orbital \otimes spin states with corresponding energies ϵ_i and ϵ_j , and the summations run over occupied (occ) and unoccupied (unocc) states, as defined by the input occupations along the global z -axis.

Appendix N: Hamiltonian Matrix Representation Before and After Spin–Orbit Coupling

1. WoV system

We construct the tight-binding Hamiltonian in the five d -orbital basis

$$\{d_{xy} \uparrow, d_{yz} \uparrow, d_{z^2} \uparrow, d_{xz} \uparrow, d_{x^2-y^2} \uparrow, d_{xy} \downarrow, d_{yz} \downarrow, d_{z^2} \downarrow, d_{xz} \downarrow, d_{x^2-y^2} \downarrow\},$$

where the first five states correspond to spin-up and the remaining five to spin-down components.

To analyze the influence of spin–orbit coupling (SOC) on the low-energy electronic structure, we constructed the model Hamiltonian both before and after including SOC effects. The non–SOC Hamiltonian (H_0) is purely diagonal, representing the orbital-resolved on-site energies, while the inclusion of SOC introduces small off-diagonal elements that couple different spin and orbital states.

The Hamiltonian before including SOC is given by:

$$H_0 = \begin{pmatrix} 4.6 & 0 & 0 & 0 & 0 & 0 & 0 & 0 & 0 & 0 \\ 0 & 5.3 & 0 & 0 & 0 & 0 & 0 & 0 & 0 & 0 \\ 0 & 0 & 5.5 & 0 & 0 & 0 & 0 & 0 & 0 & 0 \\ 0 & 0 & 0 & 4.6 & 0 & 0 & 0 & 0 & 0 & 0 \\ 0 & 0 & 0 & 0 & 5.5 & 0 & 0 & 0 & 0 & 0 \\ 0 & 0 & 0 & 0 & 0 & 4.6 & 0 & 0 & 0 & 0 \\ 0 & 0 & 0 & 0 & 0 & 0 & 5.3 & 0 & 0 & 0 \\ 0 & 0 & 0 & 0 & 0 & 0 & 0 & 5.5 & 0 & 0 \\ 0 & 0 & 0 & 0 & 0 & 0 & 0 & 0 & 4.6 & 0 \\ 0 & 0 & 0 & 0 & 0 & 0 & 0 & 0 & 0 & 5.5 \end{pmatrix} \quad (\text{N1})$$

After including the SOC interaction, the Hamiltonian becomes:

$$H = H_0 + H_{\text{SOC}} = \begin{pmatrix} 4.55 & 0 & 0 & 0.05 & 0 & 0 & 0 & 0 & 0 & 0 \\ 0 & 5.35 & 0 & 0 & 0 & 0 & 0 & 0 & 0 & 0 \\ 0 & 0 & 5.475 & 0 & 0 & 0.0612 & 0 & 0 & 0 & 0 \\ 0.05 & 0 & 0 & 4.625 & 0 & 0 & 0 & 0 & 0 & 0 \\ 0 & 0 & 0 & 0 & 5.5 & 0 & 0 & 0.0612 & 0 & 0 \\ 0 & 0 & 0.0612 & 0 & 0 & 4.6 & 0 & 0 & 0 & 0 \\ 0 & 0 & 0 & 0 & 0 & 0 & 5.325 & 0 & 0 & 0.05 \\ 0 & 0 & 0 & 0 & 0.0612 & 0 & 0 & 5.475 & 0 & 0 \\ 0 & 0 & 0 & 0 & 0 & 0 & 0 & 0 & 4.65 & 0 \\ 0 & 0 & 0 & 0 & 0 & 0 & 0.05 & 0 & 0 & 5.45 \end{pmatrix} \quad (\text{N2})$$

Here, the diagonal elements correspond to the orbital energy levels, while the small off-diagonal terms arise due to SOC-induced mixing between different orbital and spin components.

2. WV system

Hamiltonian before SOC (H_0)

In the absence of spin–orbit coupling (SOC), the Hamiltonian is diagonal, containing only the on-site energies of the d orbitals. The diagonal terms represent the crystal-field-split energies of individual orbitals, while the absence of any off-diagonal elements reflects no hybridization between orbitals in this simplified model. The corresponding Hamiltonian matrix is

The Hamiltonian before including SOC is given by:

$$H_0 = \begin{pmatrix} 5.2 & 0 & 0 & 0 & 0 & 0 & 0 & 0 & 0 & 0 \\ 0 & 4.95 & 0 & 0 & 0 & 0 & 0 & 0 & 0 & 0 \\ 0 & 0 & 5.15 & 0 & 0 & 0 & 0 & 0 & 0 & 0 \\ 0 & 0 & 0 & 5.35 & 0 & 0 & 0 & 0 & 0 & 0 \\ 0 & 0 & 0 & 0 & 5.5 & 0 & 0 & 0 & 0 & 0 \\ 0 & 0 & 0 & 0 & 0 & 5.2 & 0 & 0 & 0 & 0 \\ 0 & 0 & 0 & 0 & 0 & 0 & 4.95 & 0 & 0 & 0 \\ 0 & 0 & 0 & 0 & 0 & 0 & 0 & 5.15 & 0 & 0 \\ 0 & 0 & 0 & 0 & 0 & 0 & 0 & 0 & 5.35 & 0 \\ 0 & 0 & 0 & 0 & 0 & 0 & 0 & 0 & 0 & 5.5 \end{pmatrix} \quad (\text{N3})$$

After including the SOC interaction, the Hamiltonian becomes:

$$H = H_0 + H_{\text{SOC}} = \begin{pmatrix} 5.15 & 0 & 0 & 0.05 & 0 & 0 & 0 & 0 & 0 & 0 \\ 0 & 5.00 & 0 & 0 & 0 & 0 & 0 & 0 & 0 & 0 \\ 0 & 0 & 5.125 & 0 & 0 & 0.0612 & 0 & 0 & 0 & 0 \\ 0.05 & 0 & 0 & 5.375 & 0 & 0 & 0 & 0 & 0 & 0 \\ 0 & 0 & 0 & 0 & 5.5 & 0 & 0 & 0.0612 & 0 & 0 \\ 0 & 0 & 0.0612 & 0 & 0 & 5.2 & 0 & 0 & 0 & 0 \\ 0 & 0 & 0 & 0 & 0 & 0 & 4.975 & 0 & 0 & 0.05 \\ 0 & 0 & 0 & 0 & 0.0612 & 0 & 0 & 5.125 & 0 & 0 \\ 0 & 0 & 0 & 0 & 0 & 0 & 0 & 0 & 5.4 & 0 \\ 0 & 0 & 0 & 0 & 0 & 0 & 0.05 & 0 & 0 & 5.45 \end{pmatrix} \quad (\text{N4})$$

Here, the diagonal elements correspond to the orbital energy levels, while the small off-diagonal terms arise due to SOC-induced mixing between different orbital and spin components.

Here, the diagonal elements slightly shift compared to H_0 , reflecting SOC-induced renormalization of orbital energies, while the off-diagonal elements (typically ~ 0.05 – 0.06 eV) correspond to SOC-mediated mixing between orbitals such as (d_{xy}, d_{xz}) and (d_{z^2}, d_{xy}) . These hybridization terms are essential in generating MAE.

Appendix O: MAE Characteristics of the WoV System

In the WoV system, our density functional theory (DFT) calculations reveal that the ground state adopts a ferromagnetically noncollinear spin configuration. Taking this configuration as the magnetic ground state, we computed the partial density of states (PDOS), as displayed in Fig. 12(a). The normalized magnetic anisotropy energy (MAE), presented in Fig. 12(b), demonstrates that the z axis is no longer the easy axis of magnetization. This conclusion is further supported by Fig. 12(c), which shows a finite MAE in the xz and yz planes at 0° , confirming the deviation from z .

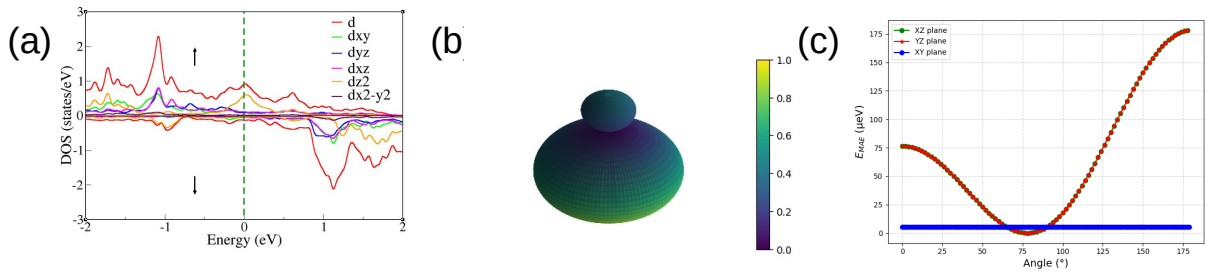


FIG. 12. (a) Partial density of states (PDOS) of Cr d orbitals for spin-up and spin-down channels. (b) Normalized magnetocrystalline anisotropy energy (MAE) on sphere. (c) MAE in different planes as a function of the polar angle.

- [1] J.-T. Wang, D.-S. Wang, C. Chen, O. Nashima, T. Kanomata, H. Mizuseki, and Y. Kawazoe, Vacancy-induced structural and magnetic transition in $\text{MnCo}_{1-x}\text{Ge}$, *Applied Physics Letters* **89**, 262504 (2006).
- [2] Z. Liu, X.-S. Ni, L. Li, H. Sun, F. Liang, B. A. Frandsen, A. D. Christianson, C. dela Cruz, Z. Xu, D.-X. Yao, J. W. Lynn, R. J. Birgeneau, K. Cao, and M. Wang, Effect of iron vacancies on magnetic order and spin dynamics of the spin ladder $\text{BaFe}_{2-\delta}\text{S}_{1.5}\text{Se}_{1.5}$, *Phys. Rev. B* **105**, 214303 (2022).
- [3] T. J. Slade, A. Sapkota, J. M. Wilde, Q. Zhang, L.-L. Wang, S. H. Lapidus, J. Schmidt, T. Heitmann, S. L. Bud'ko, and P. C. Canfield, Vacancy-tuned magnetism in LaMn_xSb_2 , *Phys. Rev. Mater.* **7**, 114203 (2023).
- [4] J. Liu, B. Ding, J. Liang, X. Li, Y. Yao, and W. Wang, Magnetic skyrmionic bubbles at room temperature and sign reversal of the topological hall effect in a layered ferromagnet $\text{Cr}_{0.87}\text{Te}$, *ACS Nano* **16**, 13911 (2022), pMID: 36000915.
- [5] R. Saha, H. L. Meyerheim, B. Göbel, B. K. Hazra, H. Deniz, K. Mohseni, V. Antonov, A. Ernst, D. Knyazev, A. Bedoya-Pinto, I. Mertig, and S. S. P. Parkin, Observation of néel-type skyrmions in acentric self-intercalated $\text{Cr}_{1+\delta}\text{Te}_2$, *Nature Communications* **13**, 3965 (2022).
- [6] C. Zhang, C. Liu, J. Zhang, Y. Yuan, Y. Wen, Y. Li, D. Zheng, Q. Zhang, Z. Hou, G. Yin, K. Liu, Y. Peng, and X.-X. Zhang, Room-temperature magnetic skyrmions and large topological hall effect in chromium telluride engineered by self-intercalation, *Advanced Materials* **35**, 2205967 (2023).
- [7] B. Rai, S. K. Kuila, R. Saha, S. Hazra, C. De, J. Sau, V. Gopalan, P. P. Jana, S. S. P. Parkin, and N. Kumar, Peculiar magnetic and magneto-transport properties in a noncentrosymmetric self-intercalated van der waals ferromagnet Cr_5Te_8 , *Chemistry of Materials* **37**, 746 (2025).
- [8] Y. Liu, Y. Liu, J. Dan, W. Liu, L. Wang, K. Hu, W. Wang, L. Zhang, B. Ge, H. Du, and D. Song, Atomic-scale order and disorder induced diverse topological spin textures in self-intercalated van der waals magnets $\text{Cr}_{1+\delta}\text{Te}_2$, *Advanced Functional Materials* **35**, 2414699 (2025).
- [9] Y. Liu and C. Petrovic, Anomalous hall effect in the trigonal Cr_5Te_8 single crystal, *Phys. Rev. B* **98**, 195122 (2018).
- [10] H. Ipser, K. L. Komarek, and K. O. Klepp, Transition metal-chalcogen systems viii: The Cr-Te phase diagram, *Journal of the Less Common Metals* **92**, 265 (1983).
- [11] Y. Fujisawa, M. Pardo-Almanza, C.-H. Hsu, A. Mohamed, K. Yamagami, A. Krishnadas, G. Chang, F.-C. Chuang, K. H. Khoo, J. Zang, A. Soumyanarayanan, and Y. Okada, Widely tunable berry curvature in the magnetic semimetal $\text{Cr}_{1+\delta}\text{Te}_2$, *Advanced Materials* **35**, 2207121 (2023).
- [12] Y. Fujisawa, M. Pardo-Almanza, J. Garland, K. Yamagami, X. Zhu, X. Chen, K. Araki, T. Takeda, M. Kobayashi, Y. Takeda, C. H. Hsu, F. C. Chuang, R. Laskowski, K. H. Khoo, A. Soumyanarayanan, and Y. Okada, Tailoring magnetism in self-intercalated $\text{Cr}_{1+\delta}\text{Te}_2$ epitaxial films, *Phys. Rev. Mater.* **4**, 114001 (2020).
- [13] M. Huang, L. Gao, Y. Zhang, X. Lei, G. Hu, J. Xiang, H. Zeng, X. Fu, Z. Zhang, G. Chai, Y. Peng, Y. Lu, H. Du, G. Chen, J. Zang, and B. Xiang, Possible topological hall effect above room temperature in layered $\text{Cr}_{1.2}\text{Te}_2$ ferromagnet, *Nano Letters* **21**, 4280 (2021), pMID: 33979154.
- [14] S. Purwar, A. Low, A. Bose, A. Narayan, and S. Thirupathaiah, Investigation of the anomalous and topological hall effects in layered monoclinic ferromagnet $\text{Cr}_{2.76}\text{Te}_4$, *Phys. Rev. Mater.* **7**, 094204 (2023).
- [15] Y. Huang, N. Zuo, Z. Zhang, X. Xing, X. Yao, A. Zhang, H. Ma, C. Xu, W. Jiao, W. Zhou, R. Sankar, D. Qian, and X. Xu, In-plane magnetic anisotropy and large topological hall effect in self-intercalated ferromagnet $\text{Cr}_{1.61}\text{Te}_2$, *Advanced Functional Materials* **n/a**, e10351 (2025).
- [16] Z. Z. Jiang, X. Liang, X. Luo, J. J. Gao, W. Wang, T. Y. Wang, X. C. Yang, X. L. Wang, L. Zhang, Y. Sun, P. Tong, J. F. Hu, W. H. Song, W. J. Lu, and Y. P. Sun, Evolution of ground state in Cr_2Te_3 single crystal under applied magnetic field, *Phys. Rev. B* **106**, 094407 (2022).
- [17] D. Feng, Z. Shen, Y. Xue, Z. Guan, R. Xiao, and C. Song, Strain-induced magnetic phase transition, magnetic anisotropy switching and bilayer antiferromagnetic skyrmions in van der waals magnet CrTe_2 , *Nanoscale* **15**, 1561 (2023).
- [18] S. Polesya, S. Mankovsky, D. Benea, H. Ebert, and W. Bensch, Finite-temperature magnetism of CrTe_2 and CrSe , *Journal of Physics: Condensed Matter* **22**, 156002 (2010).
- [19] K. He, M. Bian, S. D. Seddon, K. Jagadish, A. Mucchietto, H. Ren, E. Kirstein, R. Asadi, J. Bai, C. Yao, S. Pan, J.-X. Yu, P. Milde, C. Huai, H. Hui, J. Zang, R. Sabirianov, X. M. Cheng, G. Miao, H. Xing, Y.-T. Shao, S. A. Crooker, L. Eng, Y. Hou, J. P. Bird, and H. Zeng, Unconventional anomalous hall effect driven by self-intercalation in covalent 2d magnet Cr_2Te_3 , *Advanced Science* **12**, 2407625.
- [20] S. M. Hossain, B. Rai, P. R. Baral, O. Zaharko, N. Kumar, A. K. Bera, and M. Majumder, Evidence for magnetoelastic coupling and chiral magnetic ground state in quasi-van der waals trigonal $\text{Cr}_{1.22}\text{Te}_2$, *Phys. Rev. B* **112**, 024439 (2025).
- [21] Z.-L. Huang, W. Kockelmann, M. Telling, and W. Bensch, A neutron diffraction study of structural and magnetic properties of monoclinic Cr_5Te_8 , *Solid State Sciences* **10**, 1099 (2008).
- [22] A. F. Andresen, E. Zeppezauer, T. Boive, B. Nordström, and C. I. Brändén, The magnetic structure of Cr_2Te_3 , Cr_3Te_4 , and Cr_5Te_6 , *Acta Chemica Scandinavica* **24**, 3495 (1970).
- [23] T. Hamasaki, T. Hashimoto, Y. Yamaguchi, and H. Watanabe, Neutron diffraction study of Cr_2Te_3 single crystal, *Solid State Communications* **16**, 895 (1975).
- [24] G. Cao, Q. Zhang, M. Frontzek, W. Xie, D. Gong, G. E. Sterbinsky, and R. Jin, Structure, chromium vacancies, and magnetism in a $\text{Cr}_{12-x}\text{Te}_{16}$ compound, *Phys. Rev. Mater.* **3**, 125001 (2019).
- [25] A. F. Andresen, A neutron diffraction investigation of Cr_2Te_3 and Cr_5Te_6 , *Acta Chemica Scandinavica* **17**, 1335 (1963).

- [26] X. Chen, S. Zhang, B. Liu, F. Hu, B. Shen, and J. Sun, Theoretical investigation of magnetic anisotropy at the $\text{La}_{0.5}\text{Sr}_{0.5}\text{MnO}_3/\text{LaCoO}_{2.5}$ interface, *Phys. Rev. B* **100**, 144413 (2019).
- [27] M. Blanco-Rey, R. Castrillo-Bodero, K. Ali, P. Gargiani, F. Bertran, P. M. Sheverdyaeva, J. E. Ortega, L. Fernandez, and F. Schiller, Effect of the valence state on the band magnetocrystalline anisotropy in two-dimensional rare-earth/noble-metal compounds, *Phys. Rev. Res.* **4**, 013237 (2022).
- [28] P. Błóński, A. Lehnert, S. Dennler, S. Rusponi, M. Etzkorn, G. Moulas, P. Bencok, P. Gambardella, H. Brune, and J. Hafner, Magnetocrystalline anisotropy energy of co and fe adatoms on the (111) surfaces of pd and rh, *Phys. Rev. B* **81**, 104426 (2010).
- [29] P. Chowdhury, J. Sau, M. Numan, J. Sannigrahi, M. Gutmann, S. Giri, M. Kumar, and S. Majumdar, Suppression of intrinsic hall effect through competing berry curvature in $\text{Cr}_{1+\delta}\text{Te}_2$, *Phys. Rev. Mater.* **9**, 024407 (2025).
- [30] D. A. Keen, M. J. Gutmann, and C. C. Wilson, SXD – the single-crystal diffractometer at the ISIS spallation neutron source, *Journal of Applied Crystallography* **39**, 714 (2006).
- [31] P. Chowdhury, J. Sau, M. Numan, J. Sannigrahi, M. Gutmann, G. Das, S. Giri, M. Kumar, and S. Majumdar, Orbital degeneracy control through vacancies: A pathway to tailored magnetic state in $\text{Cr}_{1+\delta}\text{Te}_2$ (2025), **Supplemental Material**.
- [32] M. Newville, EXAFS analysis using *FEFF* and *FEFFIT*, *Journal of Synchrotron Radiation* **8**, 96 (2001).
- [33] J. Hafner, Ab-initio simulations of materials using vasp: Density-functional theory and beyond, *Journal of Computational Chemistry* **29**, 2044 (2008).
- [34] G. Kresse and D. Joubert, From ultrasoft pseudopotentials to the projector augmented-wave method, *Physical review b* **59**, 1758 (1999).
- [35] J. P. Perdew and Y. Wang, Accurate and simple analytic representation of the electron-gas correlation energy, *Phys. Rev. B* **45**, 13244 (1992).
- [36] G. Pizzi, V. Vitale, R. Arita, *et al.*, Wannier90 as a community code: new features and applications, *Journal of Physics: Condensed Matter* **32**, 165902 (2020).
- [37] N. Marzari and D. Vanderbilt, Maximally localized generalized wannier functions for composite energy bands, *Phys. Rev. B* **56**, 12847 (1997).
- [38] B. R. Judd, *Operator Techniques in Atomic Spectroscopy* (McGraw–Hill, 1963).
- [39] B. R. Cooper, R. Siemann, D. T. Cromer, and O. K. Andersen, Theory of spin-orbit-induced magnetic anisotropy, *Phys. Rev. B* **19**, 1317 (1979).
- [40] P. Bruno, Tight-binding approach to the orbital magnetic moment and magnetocrystalline anisotropy of transition-metal monolayers, *Phys. Rev. B* **39**, 865 (1989).
- [41] K. W. Song and V. I. Fal’ko, Superexchange and spin-orbit coupling in monolayer and bilayer chromium trihalides, *Phys. Rev. B* **106**, 245111 (2022).
- [42] S. Koseki, N. Matsunaga, T. Asada, M. W. Schmidt, and M. S. Gordon, Spin–orbit coupling constants in atoms and ions of transition elements: Comparison of effective core potentials, model core potentials, and all-electron methods, *The Journal of Physical Chemistry A* **123**, 2325 (2019), pMID: 30817150.
- [43] J. Sannigrahi, P. Chowdhury, D. Adroja, M. Gutmann, and S. Majumdar, *ISIS neutron and muon facility* (2025).
- [44] M. Gutmann, Sxd2001 – a program for treating data from tof neutron single-crystal diffraction, *Acta Crystallographica Section A* **61**, c164 (2005).
- [45] V. Petříček, L. Palatinus, J. Plášil, and M. Dušek, Jana2020– a new version of the crystallographic computing system jana, *Zeitschrift für Kristallographie - Crystalline Materials* **238**, 271 (2023).
- [46] A. D. Cicco, G. Aquilanti, M. Minicucci, E. Principi, N. Novello, A. Cognigni, and L. Olivi, Novel xafs capabilities at elettra synchrotron light source, *Journal of Physics: Conference Series* **190**, 012043 (2009).
- [47] B. Ravel and M. Newville, *ATHENA*, *ARTEMIS*, *HEPHAESTUS*: data analysis for X-ray absorption spectroscopy using *IFEFFIT*, *Journal of Synchrotron Radiation* **12**, 537 (2005).
- [48] M. Newville, *IFEFFIT*: interactive XAFS analysis and *FEFF* fitting, *Journal of Synchrotron Radiation* **8**, 322 (2001).
- [49] M. Aroyo, J. Perez-Mato, D. Orobengoa, E. Tasci, G. De La Flor, and A. Kirov, Crystallography online: Bilbao crystallographic server, *Bulgarian Chemical Communications* **43**, 183 – 197 (2011).
- [50] J. Perez-Mato, S. Gallego, E. Tasci, L. Elcoro, G. de la Flor, and M. Aroyo, Symmetry-based computational tools for magnetic crystallography, *Annual Review of Materials Research* **45**, 217 (2015).
- [51] J. Liu, L. Zhou, R. Liang, S. Li, Z. Li, L. Zhang, Z. Li, H. Wang, Y. Huang, R. Liu, and N. Tang, Tunable carr-type temperature dependence of uniaxial magnetocrystalline anisotropy in fe-deficient $\text{fe}_{3-x}\text{gete}_2$, *Phys. Rev. B* **111**, 144425 (2025).
- [52] W. Sucksmith and J. E. Thompson, The magnetic anisotropy of cobalt, *Proceedings of the Royal Society of London. Series A. Mathematical and Physical Sciences* **225**, 362 (1954).
- [53] C.-C. Liu, H. Jiang, and Y. Yao, Low-energy effective hamiltonian involving spin-orbit coupling in silicene and two-dimensional germanium and tin, *Phys. Rev. B* **84**, 195430 (2011).
- [54] D. Kochan, S. Irmer, and J. Fabian, Model spin-orbit coupling hamiltonians for graphene systems, *Phys. Rev. B* **95**, 165415 (2017).